Powder Technology 373 (2020) 164–173

Contents lists available at ScienceDirect

Powder Technology

journal homepage: www.elsevier.com/locate/powtec

Size and structural characterization of Si nanocrystal aggregates from a low pressure nonthermal plasma reactor

Xiaoshuang Chen [a], Takafumi Seto [b], Uwe R. Kortshagen [a], Christopher J. Hogan Jr. [a,*]

[a] Department of Mechanical Engineering, University of Minnesota, Minneapolis, MN 55455, USA
[b] Faculty of Frontier Engineering, Institute of Science and Engineering, Kanazawa University, Kanazawa, Japan

ARTICLE INFO

Article history:
Received 15 February 2020
Received in revised form 22 April 2020
Accepted 9 June 2020
Available online 22 June 2020

Keywords:
Nanocrystal
Differential mobility analysis
Aggregation
Nonthermal plasma
Spatial afterglow

ABSTRACT

Si nanocrystals (NCs) are synthesizable in low-pressure plasmas with narrow diameter distributions because of unipolar negative charging in the plasma. However, NCs must pass into a spatial afterglow, where NCs may decharge and aggregate. We use both low-pressure differential mobility analysis and quantitative TEM image analysis to examine Si NCs sampled from a 2 Torr Ar-SiH_4 plasma reactor. We find that Si NCs are incorporated into aggregates largely composed of 20 and fewer primary particles with nearly equal concentrations of negatively and positively charged NCs. The projected areas of aggregates scale with aggregate volume in similar manner to the scaling observed for aggregates from atmospheric pressure systems. Higher aggregate concentration is observed with increasing flow rate, while larger aggregate size is found with increasing precursor concentration. Measurements show that the spatial afterglow has a significant influence on the charge and extent of NC aggregation.

1. Introduction

Nonthermal plasmas are now established technology applied in the synthesis of sub-10 nm group IV semiconductor nanocrystals (NCs), with demonstrated potential to be extended to a wide variety of other materials [1–3]. Such plasmas are characterized by a non-equilibrium thermal state wherein the electron temperature can be up to several eV while other plasma species remains at room temperature [3–5]. In nonthermal plasma synthesis reactors, vapor phase precursors (or sublimated/evaporated condensed phase precursors [6,7]) chemically react, leading to nucleation and growth of the target NCs; growth reactions are facilitated by energetic plasma species. Commonly operated as flow tubes [5], in plasma synthesis systems the size distribution of the output NCs can be tuned via control of operating conditions, including flow rate, precursor concentration, neutral gas composition, operating pressure, neutral gas temperature, and plasma power. Although the synthesis reaction can be optimized for specific NC sizes by trial-and-error, detailed understanding of the nucleation and growth process in such plasma reactors is lacking, and there is interest in developing and implementing both measurement techniques [8] and theoretical analysis [9] to examine NC nucleation and growth in plasma flow tube reactors.

Interest in improved descriptions of nonthermal plasma based NC synthesis and growth processes extends beyond reactions occurring in the plasma volume, to processes affecting NCs as they pass through the boundaries of the reactor. Upon exiting a plasma, NCs are exposed to a spatial afterglow, wherein both electron and ion concentrations decay, electron temperatures decay, and there is an overall transition from a highly non-equilibrium environment to an equilibrium environment [10]. As the NCs must either be collected or deposited for eventual application or incorporation into a device, it is important to consider the possible changes in NC size distribution brought about via passage through the spatial afterglow. Within the plasma volume, unipolar negative charging via electrons can keep NCs electrically isolated from one another [11,12]; this appears to lead to the smaller polydispersity in primary NC size for nonthermal plasma synthesis [5] in comparison to higher power density plasmas [13–15], in which particles likely do not nucleate in the plasma volume but in the plasma afterglow. In a spatial plasma afterglow, depletion of electrons relative to ions can lead to reduced negative charge levels [10,16] and possibly neutralization and charge reversal for NCs, drastically increasing the aggregation rate [3,17–19]. The extent of NC aggregation and resulting aggregate structure can, in turn, affect NC transport and deposition downstream of the plasma reactor. For example, the morphologies and porosities of NC films assembled by deposition from the gas phase, as has been implemented by several groups [20–29], is directly affected by NC aggregation state prior to deposition [30,31]. Dispersal of aggregated NCs into solvents is additionally difficult without in-flight functionalization prior to the occurrence of substantial aggregation [32].

While aggregation in the post-plasma environment of atmospheric pressure microplasma synthesis reactors [17] and in microwave plasma reactors [13,14,33] has been observed and quantified, the potential for NC decharging and aggregation in the post-plasma environment of low pressure, nonthermal plasma synthesis systems has not been

* Corresponding author.
E-mail address: hogan108@umn.edu (C.J. Hogan).

https://doi.org/10.1016/j.powtec.2020.06.026
0032-5910/

probed. Motivated to better understand the effects of the post-plasma region of flow tube synthesis reactors on the synthesized NCs, in the present study we apply a combination of online and offline measurement techniques to examine the size distribution functions and structures of Si NCs synthesized in a SiH_4-Ar nonthermal plasma flow tube reactor. For online measurements we apply ion mobility spectrometry, using a uniquely designed low pressure different mobility analyzer (LPDMA) [34,35] coupled to a Faraday cage electrometer (FCE) to determine the mobility size distribution functions of NCs and NC aggregates. In prior work [35], we have demonstrated that this LPDMA can operate at pressures relevant to plasma NC synthesis (<5 Torr, where ejector based sampling [14,36] is not effective). With an appropriately applied transfer function correction scheme, LPDMA measurements can yield size distribution functions for plasma synthesized NCs akin to the size distribution function measurements traditionally made for nanoparticles synthesized in flame aerosol reactors [37,38] and made in monitoring nucleation and growth in high temperature [39] and non-equilibrium atmospheric pressure systems [40,41]. Mobility size distribution measurements have been central to understanding particle formation and growth in flames. While measurements have been demonstrated in low pressure plasma reactors previously, here we expand on prior work by varying both SiH_4 precursor concentration (partial pressure) and reactor residence time (total flow rate). Both negative and positive mode ion mobility spectra are collected and inverted to detect the presence of both residual negatively charged and charge reversed (positively charged) NCs. Mobility size distribution function inversion is coupled with structural characterization of detected Si NCs via offline transmission electron microscopy (TEM). Comparison is made to both primary NC and aggregate size distribution functions inferred from TEM measurements. In addition, from TEM images for detected NC aggregates, modeling aggregates as statistical fractals, we infer radii of gyration and the number of primary NCs per aggregate, examining the scaling between these two quantities, as well as the scaling between projected area and the aggregate volume. Measurements confirm that under all tested operating conditions, Si NCs indeed decharge and can even undergo charge reversal upon exiting a plasma reactor, facilitating NC aggregation. Measurements additionally highlight how the precursor concentration and residence time influence the NC growth process in the post-plasma environment. Comparison to TEM confirms that the LPDMA–FCE instrument combination can be used as a tool for online process monitoring of plasma NC synthesis, yielding the NC aggregate size distribution function.

2. Methods

2.1. Plasma synthesis reactor

The flow tube reactor utilized in this study is a commonly used system for the synthesis of group IV semiconductor NCs [5,42]. Briefly, as depicted in Fig. 1, Si NCs were synthesized in a flow-tube nonthermal argon plasma operating at 2 Torr (266 Pa), with SiH_4 as the silicon precursor. SiH_4 (originally in a 5% SiH_4, 95% Ar mixture) was mixed with Ar flow before entering a quartz tube reactor (1/4″ I.D., 3/8″ O.D., and 10″ length). The nucleation of Si in the plasma involves a sequence of chemical reactions, primarily silane addition to silicon hydride anions and the elimination of hydrogen. Larger particles then grow through coagulation of the initial nuclei [3]. Five distinct reactor operating conditions were examined in this study, which are noted in Table 1. These conditions were selected to yield two groups; in the first the volumetric flow rate through the reactor is held constant (constant flow residence time) and the silane volume fraction is varied, and in the second the volumetric flow rate is varied, while the silane volume fraction is held constant. Two 1-cm wide copper ring electrodes were wrapped around the plasma reactor with a 2 cm separation distance. To maintain the plasma in the tube reactor the electrodes were connected to a 10 W radiofrequency (RF) power source operated at 13.56 MHz. RF power was applied through impedance matching network. In initial design of such reactors for Si NC synthesis (though with distinct power settings) [5], the plasma (electron) density was estimated to be of the order 10^{16} m^{-3}. In comparison, the Si atomic concentration in this study was of the order 10^{18} m^{-3}. Therefore, early in the nucleation and growth process, the assumption of complete unipolar charging of nucleating NCs is not valid; presumably a significant fraction of the smallest clusters formed in reactors are neutral, though as noted, prior work [43–45] demonstrates that anionic clusters play an important role in NC nucleation.

Table 1
Experiment conditions.

SiH_4 flow rate	sccm	0.4	0.5	0.6	0.45	0.55
Ar flow rate	sccm	59.6	59.5	59.4	53.55	65.45
SiH_4 partial pressure	mTorr	13.3	16.7	20	16.7	16.7
Total flow rate	sccm	60	60	60	54	66

The ends of the tube reactor were connected to grounded ultraTorr fittings. The distance between the downstream grounded ultraTorr connector to the nearest copper ring electrode was 2 cm. We observed that the plasma extended from the electrode pair to the grounded ultraTorr fitting. A 150 square openings per linear inch wire mesh followed by a 46 square openings per linear inch wire mesh was placed 5.5 cm from the nearest plasma reactor electrode. Nucleated Si primary NCs were carried by Ar flow, partially collected by the grounded wire mesh, and then went through the LPDMA for IMS characterization or for collection for TEM measurement. The wire mesh significantly reduced NC total concentration. This effectively 'freezes' the NC size distribution function at the mesh location, because the aggregation rate scales with the square of the NC number concentration. Deposition onto the mesh occurs by both diffusion and inertial impaction at low pressure, and

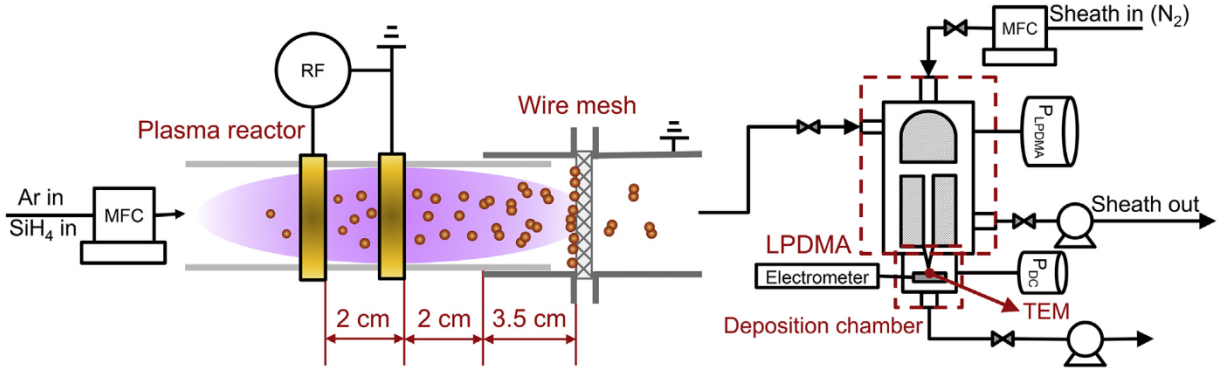

Fig. 1. A schematic diagram of the RF plasma reactor system and low pressure differential mobility analyzer utilized for size distribution measurements.

while the deposition efficiency is not corrected for in data inversion of ion mobility spectrometry measurements, it is not anticipated to strongly alter the shape of the measured size distribution functions.

2.2. Low pressure differential mobility analysis

Wire mesh filtered Ar—Si NC flow entered the LPDMA at its aerosol inlet. The operation of differential mobility analyzers is described in detail previously [34,46], and in particular the LPDMA transfer function is described previously [35]. The LPDMA was operated at the same pressure as the plasma reactor with a non-recirculating N_2 sheath flow, at a rate set at 10 times the aerosol inlet mass flow rate under all conditions. The LPDMA classification region is composed of two concentric cylinders where the inner cylinder (22 mm diameter) is connected to a high voltage DC power source and the outer cylinder (36 mm diameter) is grounded. NCs and NC aggregates migrating through the LPDMA are driven from an inlet on the outer electrode radially inward via electrostatic forces, and axially via gas flow to the outlet, which is positioned on the inner electrode, 10 mm axially downstream of the inlet position. The current of mobility-selected NCs transmitted through LPDMA was measured by the Faraday Cage electrometer attached to a deposition chamber downstream of the LPDMA outlet. By stepping the voltage of the DC power source in 4 V increments from 3 to 359 V, the mobility size distribution function of NCs was characterized in terms of the current measured (I_k) for a given applied LPDMA voltage (V_k). The mobility K_p is the proportionality coefficient between a charged NCs steady migration velocity in an electric field and the electric field strength. For the pressure range examined, it is given by the equation:

$$K_p = \frac{3ze}{\pi\xi\rho_{gas}c_{gas}}\frac{1}{(d_p+d_g)^2} \tag{1}$$

where z is the number of elementary charges on the NC, e is the elementary charge, ξ is the momentum accomodation coefficient [47], and ρ_{gas} and c_{gas} are density and thermal velocity of the neutral gas species, respectively. d_p is the mobility diameter, and d_g is the effective gas molecule diameter for the sheath gas (0.3 nm [47]). For spherical NCs, prior measurements show excellent agreement between Eq. (1) inferred diameters and the mass diameter (based on the measured particle mass and density) [47] using $\xi = 1.36$, which originally derives from the Millikan oil drop experiments [48]. At the same time, several studies [49–51] find that in the 1 nm size range, ξ may be material dependent, falling in a range from 1.2 to 1.4. While Eq. (1) has not been explicitly tested for Si, we elect to utilize $\xi = 1.36$ in this study, as is the conventional approach. This assumption could introduce an error of ~7% in the inferred mobility diameter at most (i.e., if $\xi = 1.2$). For non-spherical or aggregated entities, both theory [52] and comparison of Eq. (1) to structural features observed in electron microscopy images [53,54] reveal that the mobility diameter in reduced pressure environments coincides with an orientationally averaged, projected area equivalent diameter, hence the mobility diameter can be physically interpretted for both spherical and non-spherical NCs. The measured current is linked to the mobility size distribution function (dn/dd_p) via the equation:

$$I_k = eQ_a\sum_{z=-1}^{-\infty} z\int_0^{\infty} f(z,d_p)\frac{dn}{dd_p}\Theta_k(K_p)dd_p \tag{2}$$

where Q_a is the volumetric flow rate sampled into the LPDMA, $f(z,d_p)$ is the fraction of NCs or NC aggregates of mobility diameter d_p with z elementary charges and $\Theta_k(K_p)$ is the LPDMA transfer/transmission function with applied voltage V_k (for NCs of mobility K_p). The size distribution functions noted in Eq. (2) and provided here are given with units of m^{-4} (number concentration per unit change in diameter), such that the integral of the size distribution function yields the total number concentration measured for the charge polarity under examination. The transfer function of the LPDMA for operating conditions relevant to low pressure plasma synthesis reactors was the focus of our prior study, and is hence a known function [35]. We note that the LPDMA transfer function was developed with N_2 as both sheath and aerosol sample flow while in our experiment the aerosol flow was Ar. However, we argue that the influence of changing the composition of the inlet gas in the LPDMA transfer function is small. The exchange of aerosol inlet gas composition and sheath gas composition in DMAs was studied by Li and Chen [55], who found that the N_2—Ar aerosol-sheath gas pair has a minor influence on the evaluated particle mobility diameter in comparison with N_2-N_2 aerosol-sheath gas pair. With all parameters in Eq. (2) aside from dn/dd_p either known a priori or measured, measurement of I_k at m specified applied voltages yields m Fredholm integral equations, with which an inversion method can be applied to yield dn/dd_p [56]. However, as noted in the introduction, the charge distribution is uncertain following the plasma reactor. In typical aerosol measurements, the charge distribution is modulated prior to ion mobility spectrometry via exposing particles to roughly equal concentrations of positive and negative ions; after sufficient time this leads to a steady state where $f(z, d_p)$ can be reasonably approximated [57,58]. While particle charge conditioning approaches have been developed for low pressure conditions [59,60], such devices are not readily available (i.e., they are rather unique), and furthermore, in the current study we sought to use ion mobility measurements to obtain information about the post-plasma NC charge distribution. Therefore, in inverting mobility size distribution functions, for both negatively charged NCs and positively charged NCs (for which Eq. (2) is summed from $z = +1$ to $+\infty$ instead of over negative charge states), we assumed all detected NCs and NC aggregates were singly charged ($z = +1$ or $z = -1$ only), reporting distinct positively and negatively charged mobility size distributions. A second implicit assumption made with this approximation is that the fractions of $z = +1$ and $z = -1$ NCs are weakly size-dependent, such that the distribution function shapes inverted from positive and negative mode measurements reflect the true distribution function. The assumptions of singly charged NCs and size-independent charge fractions are scrutinized subsequently through comparison of mobility size distribution functions to those inferred from TEM analysis; the latter does not require any assumptions regarding NC elementary charge states and charge fractions. Measurements of positively and negatively charged NCs were conducted by switching the polarity of DC power source used in operating the LPDMA. All the LPDMA measurements were conducted in duplicate for each charge state, in a manner alternating between positively and negatively charged NCs. A Twomey-Markowski algorithm [56], as described previously [35], was used to solve the system of equations brought about by measurements, yielding mobility size distribution functions.

2.3. Transmission electron microscopy

TEM samples of Si NCs were collected on carbon coated copper grids (Ted Pella, Inc. 01803-F), which were placed in the LPDMA deposition chamber as shown in Fig. 1. During sample collection, NCs synthesized from the plasma reactor were again partially collected by the wire mesh in the same manner as in LPDMA measurements, but were deposited on TEM grids downstream of the LPDMA without LPDMA selection, that is the LPDMA sheath flow and voltage were turned off during TEM collection. Collection was carried out for ~2 s only in order to limit deposition induced aggregation [61]. TEM images were collected with a FEI Tecnai T12 transmission electron microscope at the University of Minnesota Characterization Facility with a 120 kV accelerating voltage. The primary NC diameters (d_0) were measured manually with ImageJ software. Aggregates were observed in TEM images, and to quantify their structural features possible three-dimensional NC aggregate properties were inferred with the aid of an in-house written MATLAB program. While there has been considerable recent progress [62,63] in developing methods to analyze aggregate morphologies from TEM images, we note that the method we describe and apply in this work is

distinct in that we first attempt to identify probable three-dimensional structures for aggregates, and then examine properties of the estimate three-dimensional structures collectively, as opposed to directly examining the calculated properties of the two-dimensional projections. Specifically, as described by Thajudeen et al. [53], first, we used the in-house written MATLAB program to identify individual NC aggregates and to calculate the perimeter, projection area, longest-end-to-end distance, and two-dimensional radius of gyration for each (the projection descriptors). Second, we assume each aggregate can be modeled as a statistical fractal, approximately satisfying the equation:

$$R_g = a_{base}\left(\frac{N}{k_f}\right)^{1/D_f} \tag{3}$$

where R_g is the three-dimensional radius of gyration, N is the base spherical units comprising the aggregate, a_{base} is the base unit radius of the spheres used to construct the aggregate, D_f is the fractal dimension, and k_f is a pre-exponential factor. D_f, which ranges from 1.0 for a straight chain to 3.0 for a densely packed architecture, quantifies how branched the aggregate is, while k_f is linked to the width or thickness of the branches relative to a_{base}. Simulated aggregates satisfying Eq. (3) were computationally generated using the cluster–cluster algorithm described by Filippov et al. [64], with prescribed N, k_f, and D_f inputs. We examined the range $N < 1000$, $1.3 \le D_f \le 2.9$ (with Filippov et al. [64] sequential algorithm used for fractal dimension above 2.7), and $1.3 \le k_f \le 2.0$. The deposition of each computationally generated aggregate was then simulated for 10 randomly selected orientations (leading to more than 60 000 projections, in total) and the four projection descriptors were calculated for each computationally generated projection. For computationally generated projections, a_{base} is taken to be a dimensionless unit value. In analyzing aggregate projections in TEM images, a_{base} is determined via a thresholding algorithm. As discussed in prior studies examining TEM-inferred primary particle size distribution functions [65,66], a_{base} determined via thresholding is not equivalent to the true primary particle radius; here we commonly observed it to be a factor 2–3 times smaller than the manually measured primary particle radius. For this reason, a_{base} is only used in comparing the TEM-observed projection descriptors to those for computationally-generated aggregates. We consequently only report large scale aggregate descriptors (radius of gyration, projected area, and volume), which are not strongly dependent on a_{base} (i.e., they are dimensional). Normalizing TEM-observed projection descriptors by a_{base} (the projection area is normalized by πa_{base}^2), we then utilized the error weighted averaging approach of Jeon et al. [67] to determine the most probable values of N, k_f, D_f, and the orientationally averaged projected area ($\overline{A_p}$, calculated via the algorithm provided by Gopalakrishnan et al. [68]) for each TEM observed aggregate. With N, k_f, D_f determined, we then determined each aggregate's radius of gyration (R_g) via Eq. (3) and each aggregate's volume via the relationship $V = N\frac{4\pi}{3}a_{base}^3$. 663 total aggregates (across the five measurement conditions) were examined in this manner. From the orientationally averaged projected area we also inferred the mobility diameter [54] (i.e., $d_p = \left(4\overline{A_p}/\pi\right)^{1/2}$), and by binning observed aggregates in mobility diameter we created TEM-inferred mobility size distribution functions. Subsequently, we compare both the primary NC size distribution functions and the TEM based mobility size distribution functions to ion mobility spectrometry results for all examined plasma reactor operating conditions.

3. Results and discussion

3.1. Aggregate structural characterization

We elect to present offline TEM based aggregate characterization prior to discussing ion mobility spectrometry measurements as we compare size distributions from ion mobility spectrometry to those inferred from TEM, and we extract structural descriptions of NCs from TEM. Selected TEM images of Si NCs collected under the five utilized operating conditions are shown in Fig. 2, along with a zoomed-in image revealing the lattice structure of crystalline Si. Under all examined conditions, Si NC aggregates composed of multiple primary Si NCs are evident along with several isolated primary NCs. This suggests that Si NC aggregation does in fact occur within the flow tube reactor lines, and while aggregation within the plasma volume cannot be completely ruled out [9], it is more likely to occur within the spatial afterglow region. For the aggregates examined via quantitative TEM image analysis, normalized NC aggregate volumes (noted as V^*) are plotted versus the primary NC normalized radii of gyration in Fig. 3a. Volume normalization is carried out with the manually determined primary NC volume ($d_0 = 6.8$ nm, assuming spherical NCs); the normalized volume is representative of the number of primary NCs in each imaged aggregate. Values less than one indicate isolated primary NCs or small aggregates composed of primary NCs smaller than the mean size. Diffusion and ballistic limited cluster–cluster aggregation simulations [69,70] and experiments [71,72] typically show that in the absence of external forces and without aggregate restructuring or coalescence, the number of primary particles in an aggregate scales with the radius of gyration raised to a power of 1.7–2.0 (the Hausdorff fractal dimension). Most of the aggregates observed in this work had volumes equivalent to 20 primary NCs or fewer, which is smaller than typically examined in prior simulations in experiments, where the aggregates often were composed of 10^2–10^3 primary spheres. Correspondingly, the scaling between normalized volume and normalized radius of gyration observed here is weaker than in studies of larger aggregates. At the same time, highly similar results are observed for all tested synthesis conditions, and while a very narrow range of operating space is examined in this study, this suggests that aggregation occurs in a similar manner in all instances. The experimental range is limited because the particle signal needs to be higher than the noise level of the FCE yet low enough to avoid clogging on the LPDMA detection slit. The limitation is also attributable to the need to vary the total flow rate through the reactor while keeping the pressure constant and balancing the sheath-to-aerosol inlet flow rate ratio for proper measurements.

Inferred, orientationally averaged projected areas (normalized by the projected area of a primary NC) are plotted versus normalized aggregate volumes in Fig. 3b. Scaling between the normalized projected area and normalized volume is noticeably clearer than the scaling between volume and radius of gyration. Similar observations were made by Thajudeen et al. [73] in simulating aggregation in the transition regime in the absence of coalescence and particle–particle interactions; they observed that independent of the simulation temperature and pressures (which were represented dimensionlessly), a clear scaling for all aggregates between projected area and normalized volume emerged. For this reason, in Fig. 3c we plot a comparison of the projected area versus normalized volume results obtained here to Thajudeen et al. [73] simulation results, Thajudeen et al. [53] inferred results for TiO_2 nanoparticle aggregates synthesized in an atmospheric pressure flame reactor, and Chen et al. [17] inferred results for aggregates formed via the decomposition of nickelocene in an atmospheric pressure microplasma. Although we report on smaller aggregates in this study (as aggregation is mitigated after the mesh collectors), the combined set of simulation and experimental measurements shows a single scaling between normalized area and volume ($\overline{A_p}V^{0.90}$). The slight offset for the results presented here is likely attributable to the lower numbers of primary NCs per aggregate, as well as the numerous approximations made in the image analysis approach employed. This strong agreement with prior work suggests that the aggregation of NCs

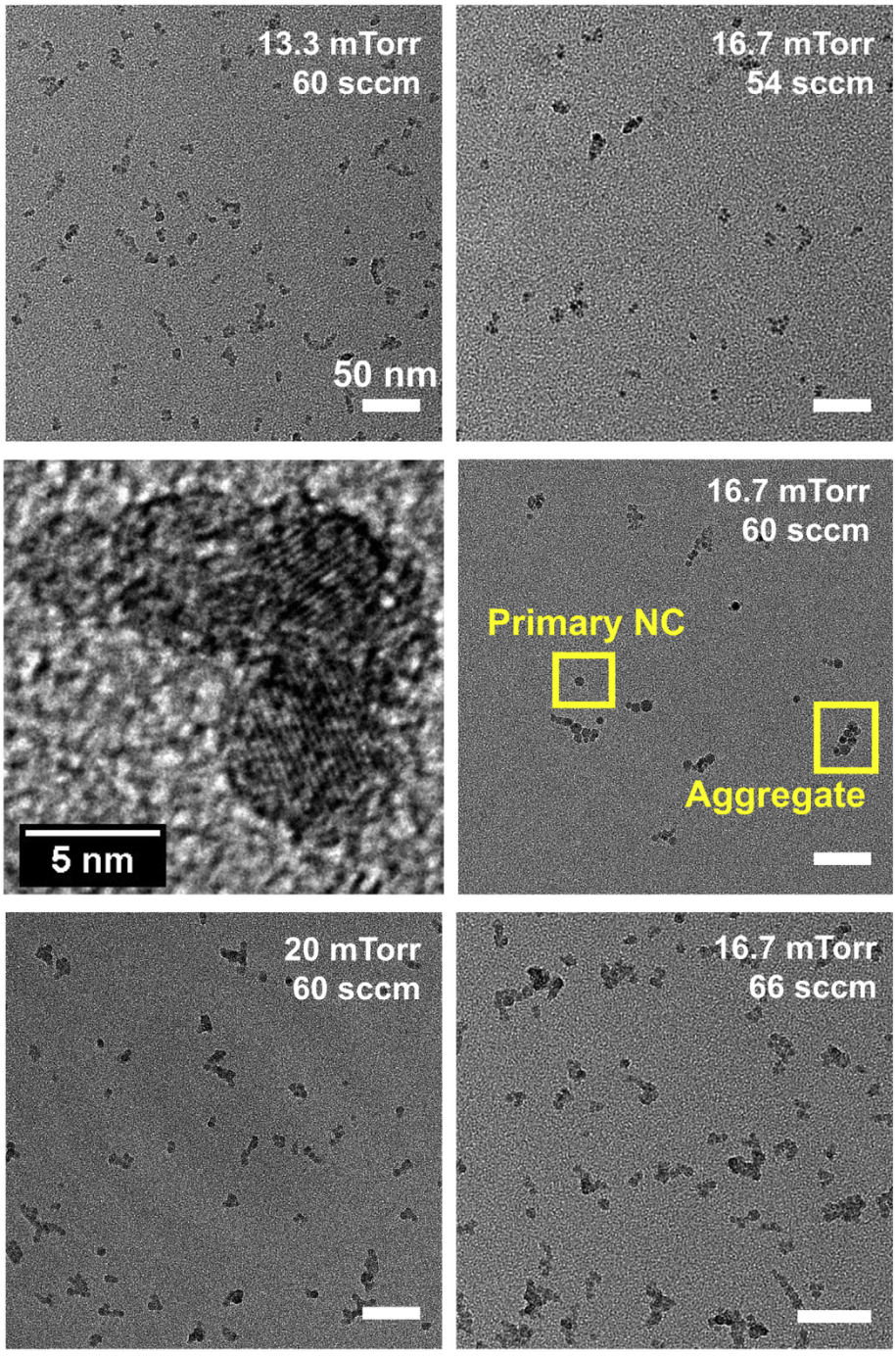

Fig. 2. Representative TEM images of the synthesized Si NCs under all examined operating conditions, and a demonstration of primary NC and aggregate definitions. The middle-left figure is a zoomed-in image of a Si NC aggregate at 16.7 mTorr silane partial pressure and 60 sccm total flow rate synthesis condition; the spacing of the fringes is 0.31 nm, which corresponds to the (111) plane in diamond cubic silicon. In all other images, the scale bar is 50 nm.

synthesized in nonthermal plasma reactor systems is not unique from other gas phase processes in higher pressure environments, and equilibrium environments. Also noteworthy is that aggregation can be described as a ballistic (free molecular) process in the low pressure reactor examined, while all other results plotted in Fig. 3c apply for systems outside the ballistic limit, where the Knudsen numbers defining growth evolve from free molecular to continuum (the transition regime). In spite of this difference in environment, aggregate projected area scales similarly with volume across multiple decades in normalized volume.

3.2. Aggregate and primary nanocrystal size distributions

Fig. 4 displays a combined plot of the unprocessed mobility spectra from the LPDMA (current as a function of mobility diameter, assuming singly charged NCs and NC aggregates), the inverted size distribution functions, manually determined primary NC diameter distributions (from TEM), and mobility based size distributions constructed by binning results from aggregate image analysis. Integrals of the latter two result in the total number of primary NCs and aggregates counted, respecitively. Comparison to TEM based distributions

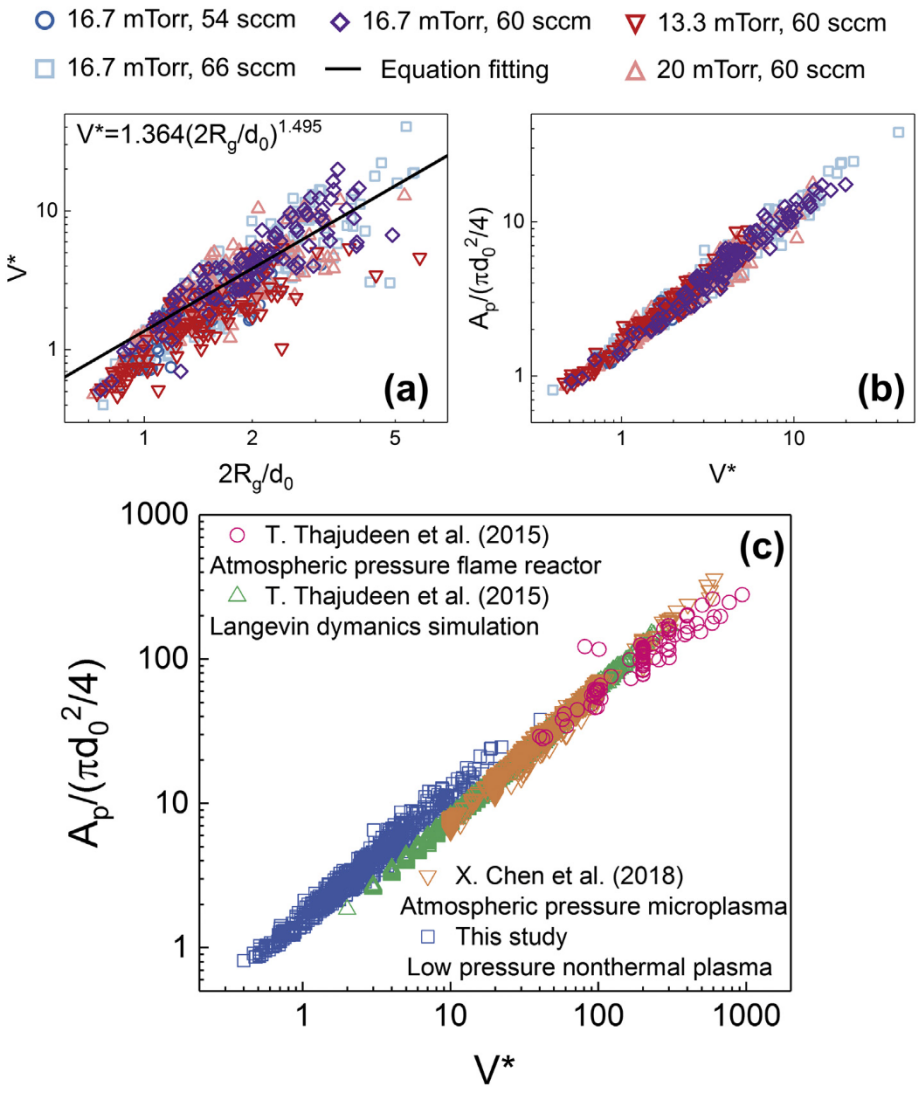

Fig. 3. A plot of the normalized volumes of aggregates inferred from image analysis versus normalized radii of gyration (a), a plot of the inferred orientationally averaged projected areas versus normalized volumes (b), and a comparison (c) of the projected area versus normalized volume scaling observed here to the simulation results of Thajudeen et al. [73], the experimentally inferred values of Thajudeen et al. [53] for TiO_2 in an atmospheric pressure flame synthesis system, and the experimentally inferred values of Chen et al. [17] for aggregates formed via the decomposition of nickelocene in an atmospheric pressure microplasma.

long these lines is a common approach to examine the performance of low pressure particle analysis instruments [74]. LPDMA based results are shown for both negatively and positively charged NCs. Data inversion corrects for the influences of the mobility analyzer tranmission efficiency. In general inverted curves are modestly shifted to smaller sizes as such NCs are transmitted less efficiently through the device. Immeditately apparent, even prior to data inversion, is that both negatively and positively charged NCs are detected downstream of the synthesis reactor under all conditions; in fact negatively and positively charged NCs are sampled in nearly equal concentrations. This finding is consistent with our preliminary mobility measurements of Si NCs from nonthermal plasma reactors [35]. It is also consistent with the findings of van Minderhout et al. [16], who examined the charge distributions on microparticles in a spatial afterglow. While they found consistently negatively charged particles, the level of charge was orders magnitude below the expected level within the plasma volume, suggesting rapid decharging in the afterglow. We observe not only decharging, but charge reversal, as the Si NC and NC aggregates examined appear to have a nearly symmetric, bipolar charge distribution. As noted in the methods section, inversion was carried out separately for negatively and positively charged NCs assuming singly charged NCs and aggregates. With this assumption, the LPDMA based mobility size distribution functions and those inferred from TEM analysis for aggregates are in excellent agreement with each another for all measurement conditions (with slight disagreement for the 16.7 mTorr, 60 sccm flow rate measurement condition). This internal consistency supports both the singly charged assumption, the weak size-dependency of the charge fraction over the narrow-size range examined, and the application of three dimensional aggregate reconstruction from TEM aggregate projections. If NCs were multiply charged, the peak location of TEM size distribution functions would be multiple times of that of the LPDMA inverted mobility size distribution functions. As can be seen from Eq. (1), neglecting the addition of the gas molecule diameter, the mobility diameter of a doubly-charged NC is $\sqrt{2}$ times that of a singly-charged NC and there would be much poorer agreement in mobility size distribution function and TEM inferred count distribution mode diameters if a large fraction of multiply charged NCs were present. While future, theoretical, numerical, and experimental studies of the spatial afterglow environment will be necessary in order to understand how NC and NC aggregates can not only decharge, but can become positively charged, in total we

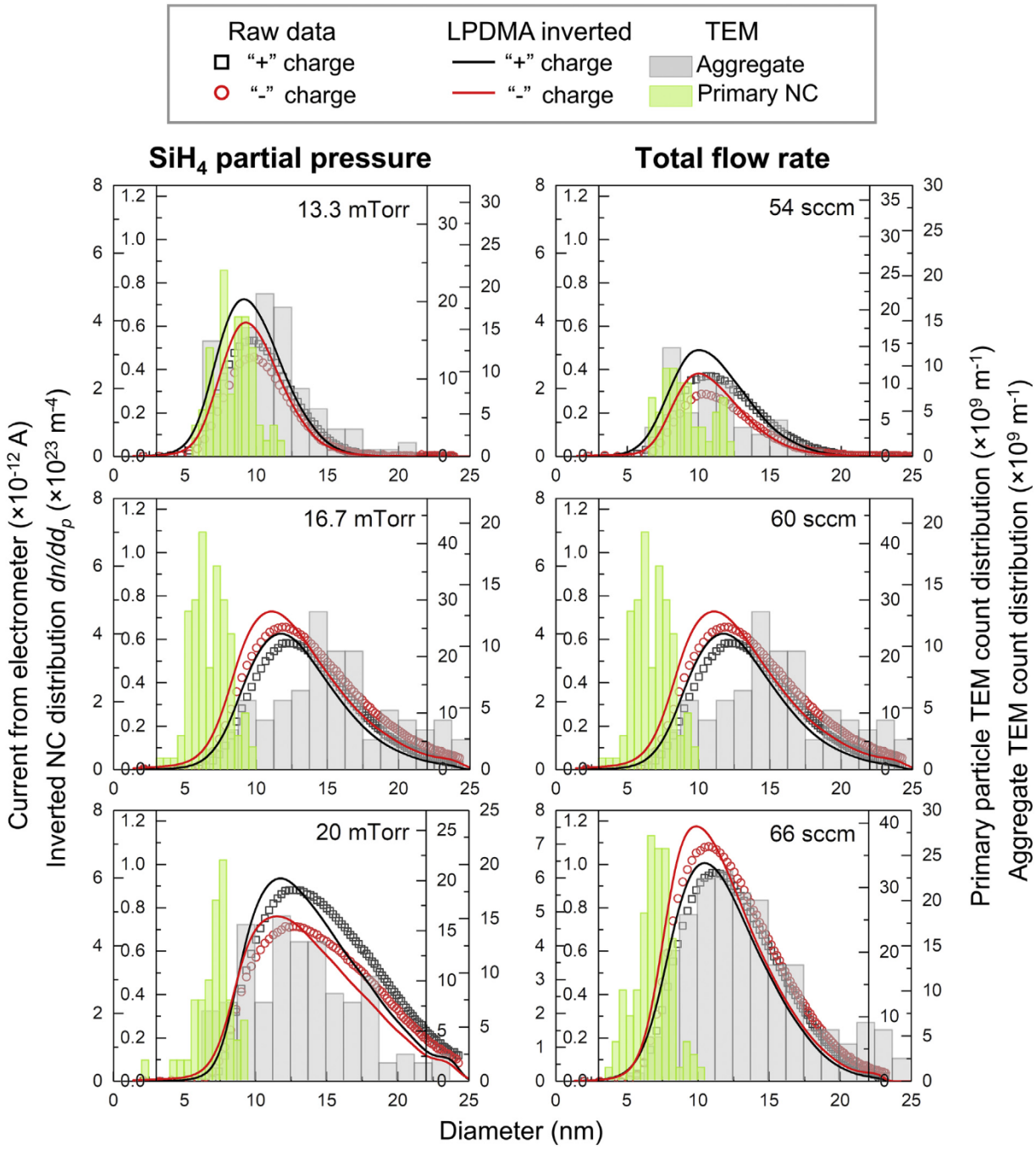

Fig. 4. A summary of LPDMA measurement results in comparison to TEM measurement results for all examined reactor conditions. Results plotted in the left column correspond to measurements for fixed reactor volumetric flow rate (60 sccm) and variable SiH_4 partial pressure (at a total reactor pressure of 2 Torr), and results plotted in the right column correspond to SiH_4 partial pressures of 16.7 mTorr, at variable total reactor volumetric flow rate. Directly measured LPDMA signal and inverted mobility size distribution functions are plotted for both positively and negatively charged NCs, and compared to both primary NC diameter count distributions determined via manual TEM measurements as well as mobility size distributions inferred via aggregate image analysis.

find that the presence of bipolarly charged aggregates is supported by both ion mobility spectrometry and TEM measurements.

3.3. Reactor operating condition influences

After establishing that LPDMA–FCE measurements yield mobility size distribution functions of bipolarly charged Si NC aggregates, we examine how resulting mobility sizes are affected by changes to SiH_4 partial pressure and reactor flow rate. The mean mobility diameter and primary NC diameter are plotted in Fig. 5 varying these two parameters, while holding the other parameters fixed, including the total plasma power. To interpret these results, it is instructive to discuss what is commonly observed in equilibrium, high temperature gas phase reactors. Typically, the aggregate mobility diameter increases with increasing precursor concentration and decreases with increasing reactor flow rate. The aggregate number concentration is less sensitive to precursor concentration, while increasing the flow rate leads to higher number concentrations of aggregates (which are smaller). In probing aggregation of particles at the outlet of an atmospheric pressure microplasma reactor [17], we observed aggregation largely consistent with this

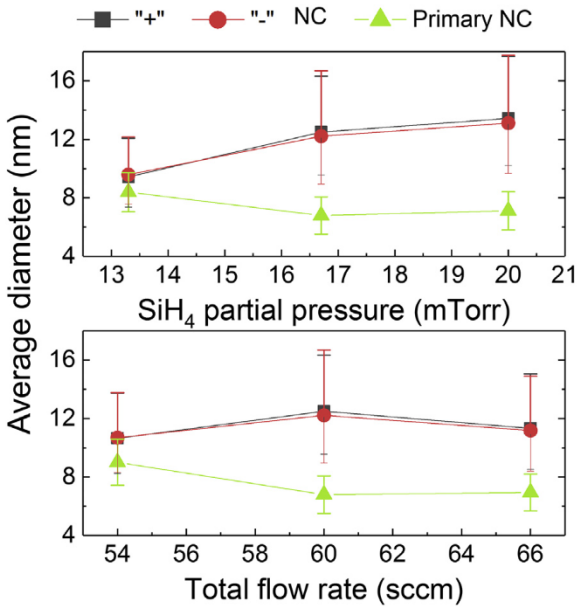

Fig. 5. The average mobility diameters and primary NC diameters as functions of SiH_4 partial pressure at a total reactor flow rate of 60 sccm and as functions of total reactor flow rate at a SiH_4 partial pressure of 16.7 mTorr. The average diameter of the NC is the geometric mean diameter of the LPDMA inverted size distributions with error bars showing the extent spanned by the geometric standard deviation of the size distribution function; the average diameter of primary NC is the arithmetic mean diameter from TEM measurement with error bars showing standard deviation.

depiction; as precursor concentration increased both aggregate size and number concentration increased, while as flow rate increased, aggregate size decreased while number concentration increased. Consistent with the finding in atmospheric pressure, with increasing SiH_4 partial pressure, here we find that mean aggregate mobility size increases (by nearly 33% over the narrow parameter space examined) and by examining inverted size distribution functions in Fig. 4, the aggregate number concentration is found to be relatively insensitive to SiH_4 partial pressure. However, with increasing system flow rate, the NC aggregate mean mobility size is found invariant, while there is a substantial increase in aggregate number concentration (by nearly a factor of 2 as the reactor flow rate increases from 54 to 66 sccm). We attribute this to decreased Si NC deposition and decreased precursor and cluster reaction on the reactor walls with decreased residence time, suggesting that in nonthermal plasma synthesis the NC synthesis reaction is in direct competition with deposition and film growth reactions (i.e., flow tube reactors are the inverse of plasma enhanced chemical vapor deposition systems, wherein NCs are a contaminant).

All reactor operating conditions yield similar primary NC diameter distributions, with the mean diameter actually decreasing slightly with increasing precursor concentration. The primary NC diameter is controlled by nucleation and surface growth reactions in the plasma volume [45], and it unfortunately appears that LPDMA–FCE measurements cannot be correlated with primary NC diameter distributions. Nonetheless, because the mobility diameter is a measure of aggregate size and because proper data inversion yields quantitative distribution functions, we propose that LPDMA–FCE measurements can be used for online characterization in non-thermal synthesis systems; both the increase aggregate mobility sizes and number concentrations are indicative of higher yields. Furthermore, in conjunction with TEM analysis of primary NCs, LPDMA–FCE measurements can be used to quantify the structure of aggregates formed, enabling prediction [29,30,75] of the morphologies of films produced via NC deposition, and ultimately prediction of NC film properties [76,77].

4. Conclusions

Low pressure, nonthermal plasma flow tube reactors enable the production of NCs with narrow primary NC diameter distributions, but as NCs must pass through a spatial afterglow for collection or subsequent gas phase functionalization, there is the potential for decharging and aggregation. We have applied a combination of ion mobility spectrometry and quantitative image analysis to show that the NCs are not unipolarly negative following passage through a spatial afterglow and in fact those detected are primarily singly charged, both negatively and positively. This also suggests that most NCs are neutral, though neutral NCs cannot be examined via ion mobility spectrometry. NCs are further grouped into small aggregates, largely composed of 20 primary NCs or fewer, whose projected areas, and hence mobility diameters, scale similarly with number of primary NCs (normalized volume) as aggregates sampled from atmospheric pressure systems [17,53] and computationally generated aggregates [73] from Langevin simulations. While ion mobility spectrometry does not yield primary NC diameter distributions, it can be used to monitor the extent of aggregation and aggregation size distribution; this, in turn, yields the NC aggregate diffusion coefficients and enables prediction of NC aggregate transport and deposition.

Future studies to gain further insight into the NC growth processes in low pressure plasmas may also utilize ion mobility spectrometry. While the measurements made in the present study focused on NCs with diameters above 4 nm and were carried out using a modest resolving power differential mobility analyzer, high resolution drift tube technology [78,79], or higher resolution differential mobility analyzers [80] optimized for the operating pressure of low pressure plasmas, may enable detection and characterization of growing nanoclusters (~1 nm in characteristic size) in plasma reactors. Such characterization would need to be coupled with improved sampling techniques to examine species as they persist in the plasma volume, as the present work shows that the spatial afterglow has a direct influence on the NC agglomeration at the exit of plasma flow tube reactors.

Declaration of Competing Interest

There are no conflicts to declare.

Acknowledgements

The manufacture of the low pressure differential mobility analyzer was supported primarily by the National Science Foundation through the University of Minnesota MRSEC under Award Number DMR-1420013. TEM characterization was carried out at the University of Minnesota Characterization facility, which is also supported by the University of Minnesota MRSEC. X.C. was additionally supported by Department of Energy Award SC0018202.

References

[1] U. Kortshagen, Nonthermal plasma synthesis of nanocrystals: fundamentals, applications, and future research needs, Plasma Chem. Plasma Process. 36 (2016) 73–84.
[2] A. Alvarez Barragan, N.V. Ilawe, L. Zhong, B.M. Wong, L. Mangolini, A non-thermal plasma route to plasmonic TiN nanoparticles, J. Phys. Chem. C 121 (2017) 2316–2322.
[3] U.R. Kortshagen, R.M. Sankaran, R.N. Pereira, S.L. Girshick, J.J. Wu, E.S. Aydil, Nonthermal plasma synthesis of nanocrystals: fundamental principles, materials, and applications, Chem. Rev. 116 (2016) 11061–11127.
[4] L. Mangolini, U. Kortshagen, Selective nanoparticle heating: another form of non-equilibrium in dusty plasmas, Phys. Rev. E 79 (2009).
[5] L. Mangolini, E. Thimsen, U. Kortshagen, High-yield plasma synthesis of luminescent silicon nanocrystals, Nano Lett. 5 (2005) 655–659.
[6] N.B. Uner, D.M. Niedzwiedzki, E. Thimsen, Nonequilibrium plasma aerotaxy of InN nanocrystals and their photonic properties, J. Phys. Chem. C 123 (2019) 30613–30622.
[7] N.B. Uner, E. Thimsen, Nonequilibrium plasma aerotaxy of size controlled GaN nanocrystals, J. Phys. D. Appl. Phys. 53 (2019) 95201.
[8] L. Mangolini, Monitoring non-thermal plasma processes for nanoparticle synthesis, J. Phys. D. Appl. Phys. 50 (2017) 373003.

[9] S.L. Girshick, Particle nucleation and growth in dusty plasmas: on the importance of charged-neutral interactions, J. Vac. Sci. Technol. A 38 (2019) 11001.
[10] L. Couëdel, A.A. Samarian, M. Mikikian, L. Boufendi, Influence of the ambipolar-to-free diffusion transition on dust particle charge in a complex plasma afterglow, Phys. Plasmas 15 (2008) 63705.
[11] T. Matsoukas, M. Russell, Particle charging in low-pressure plasmas, J. Appl. Phys. 77 (1995) 4285–4292.
[12] M. Gatti, U. Kortshagen, Analytical model of particle charging in plasmas over a wide range of collisionality, Phys. Rev. E 78 (2008) 46402.
[13] F. Kunze, S. Kuns, M. Spree, T. Hülser, C. Schulz, H. Wiggers, S.M. Schnurre, Synthesis of silicon nanoparticles in a pilot-plant-scale microwave plasma reactor: impact of flow rates and precursor concentration on the nanoparticle size and aggregation, Powder Technol. 342 (2019) 880–886.
[14] T. Rosenberger, A. Münzer, D. Kiesler, H. Wiggers, F.E. Kruis, Ejector-based sampling from low-pressure aerosol reactors, J. Aerosol Sci. 123 (2018) 105–115.
[15] M. Leparoux, C. Schreuders, J.W. Shin, S. Siegmann, Induction plasma synthesis of carbide nano-powders, Adv. Eng. Mater. 7 (2005) 349–353.
[16] B. van Minderhout, T. Peijnenburg, P. Blom, J.M. Vogels, G.M.W. Kroesen, J. Beckers, The charge of micro-particles in a low pressure spatial plasma afterglow, J. Phys. D. Appl. Phys. 52 (2019) 32LT03.
[17] X. Chen, S. Ghosh, D.T. Buckley, R.M. Sankaran, C.J. Hogan, Characterization of the state of nanoparticle aggregation in non-equilibrium plasma synthesis systems, J. Phys. D. Appl. Phys. 51 (2018) 335203.
[18] B. Santos, L. Cacot, C. Boucher, F. Vidal, Electrostatic enhancement factor for the coagulation of silicon nanoparticles in low-temperature plasmas, Plasma Sources Sci. Technol. 28 (2019) 45002.
[19] U. Kortshagen, U. Bhandarkar, Modeling of particulate coagulation in low pressure plasmas, Phys. Rev. E 60 (1999) 887–898.
[20] Z.C. Holman, U.R. Kortshagen, A flexible method for depositing dense nanocrystal thin films: impaction of germanium nanocrystals, Nanotechnology 21 (2010) 335302.
[21] P. Firth, Z.C. Holman, Aerosol impaction-driven assembly system for the production of uniform nanoparticle thin films with independently tunable thickness and porosity, ACS Appl. Nano Mater. 1 (2018) 4351–4357.
[22] E. Thimsen, M. Johnson, X. Zhang, A.J. Wagner, K.A. Mkhoyan, U.R. Kortshagen, E.S. Aydil, High electron mobility in thin films formed via supersonic impact deposition of nanocrystals synthesized in nonthermal plasmas, Nat. Commun. 5 (2014) 5822.
[23] K. Wegner, P. Piseri, H.V. Tafreshi, P. Milani, Cluster beam deposition: a tool for nanoscale science and technology, J. Phys. D. Appl. Phys. 39 (2006) R439–R459.
[24] T.L. Koh, M.J. Gordon, Spray deposition of nanostructured metal films using hydrodynamically stabilized, high pressure microplasmas, J. Vac. Sci. Technol. A 31 (2013) 61312.
[25] J. Ma, M.F. Becker, J.W. Keto, D. Kovar, Laser ablation of nanoparticles and nanoparticulate, thick Fe1.92Tb0.3Dy0.7 films, J. Mater. Res. 25 (2010) 1733–1740.
[26] M. Adachi, K. Okuyama, Y. Kousaka, H. Tanaka, Preparation of gas sensitive film by deposition of ultrafine tin dioxide particles, J. Aerosol Sci. 19 (1988) 253–263.
[27] N.P. Rao, H.J. Lee, M. Kelkar, D.J. Hansen, J.V.R. Heberlein, P.H. McMurry, S.L. Girshick, Nanostructured materials production by hypersonic plasma particle deposition, Nanostruct. Mater. 9 (1997) 129–132.
[28] S. Ghosh, X. Chen, C. Li, B.A. Olson, C.J. Hogan Jr., Fragmentation and film growth in supersonic nanoaggregate aerosol deposition, AIChE Journal (2019) e16874.
[29] N. Nasiri, T.D. Elmøe, Y. Liu, Q.H. Qin, A. Tricoli, Self-assembly dynamics and accumulation mechanisms of ultra-fine nanoparticles, Nanoscale 7 (2015) 9859–9867.
[30] L. Mädler, A.A. Lall, S.K. Friedlander, One-step aerosol synthesis of nanoparticle agglomerate films: simulation of film porosity and thickness, Nanotechnology 17 (2006) 4783–4795.
[31] S. Salameh, R. Scholz, J.W. Seo, L. Mädler, Contact behavior of size fractionated TiO2 nanoparticle agglomerates and aggregates, Powder Technol. 256 (2014) 345–351.
[32] Z. Li, U.R. Kortshagen, Aerosol-phase synthesis and processing of luminescent silicon nanocrystals, Chem. Mater. 31 (2019) 8451–8458.
[33] J. Knipping, H. Wiggers, B. Rellinghaus, P. Roth, D. Konjhodzic, C. Meier, Synthesis of high purity silicon nanoparticles in a low pressure microwave reactor, J. Nanosci. Nanotechnol. 4 (2004) 1039–1044.
[34] T. Seto, T. Nakamoto, K. Okuyama, M. Adachi, Y. Kuga, K. Takeuchi, Size distribution measurement of nanometer-sized aerosol particles using dma under low-pressure conditions, J. Aerosol Sci. 28 (1997) 193–206.
[35] X. Chen, T. Seto, U.R. Kortshagen, C.J. Hogan, Determination of nanoparticle collision cross section distribution functions in low pressure plasma synthesis reactors via ion mobility spectrometry, Nano Futures 3 (2019) 15002.
[36] J. Holm, J.T. Roberts, Surface chemistry of aerosolized silicon nanoparticles: evolution and desorption of hydrogen from 6-nm diameter particles, J. Am. Chem. Soc. 129 (2007) 2496–2503.
[37] E. Thimsen, P. Biswas, Nanostructured photoactive films synthesized by a flame aerosol reactor, AIChE J. 53 (2007) 1727–1735.
[38] H. Lin, C. Gu, J. Camacho, B. Lin, C. Shao, R. Li, H. Gu, B. Guan, H. Wang, Z. Huang, Mobility size distributions of soot in premixed propene flames, Combust. Flame 172 (2016) 365–373.
[39] M. Vazquez-Pufleau, Y. Wang, P. Biswas, E. Thimsen, Measurement of sub-2 nm stable clusters during silane pyrolysis in a furnace aerosol reactor, J. Chem. Phys. 152 (2020) 24304.
[40] A. Kumar, S. Kang, C. Larriba-Andaluz, H. Ouyang, C.J. Hogan, R.M. Sankaran, Ligand-free Ni nanocluster formation at atmospheric pressure via rapid quenching in a microplasma process, Nanotechnology 25 (2014) 385601.
[41] S. Ghosh, T. Liu, M. Bilici, J. Cole, I.M. Huang, D. Staack, D. Mariotti, R.M. Sankaran, Atmospheric-pressure dielectric barrier discharge with capillary injection for gas-phase nanoparticle synthesis, J. Phys. D Appl. Phys. 48 (2015) 314003.
[42] R. Gresback, Z. Holman, U. Kortshagen, Nonthermal plasma synthesis of size-controlled, monodisperse, freestanding germanium nanocrystals, Appl. Phys. Lett. 91 (2007) 93119.
[43] A.A. Howling, L. Sansonnens, J.L. Dorier, C. Hollenstein, Negative hydrogenated silicon ion clusters as particle precursors in RF silane plasma deposition experiments, J. Phys. D. Appl. Phys. 26 (1993) 1003–1006.
[44] S.J. Choi, M.J. Kushner, The role of negative ions in the formation of particles in low-pressure plasmas, J. Appl. Phys. 74 (1993) 853–861.
[45] U.V. Bhandarkar, M.T. Swihart, S.L. Girshick, U.R. Kortshagen, Modelling of silicon hydride clustering in a low-pressure silane plasma, J. Phys. D. Appl. Phys. 33 (2000) 2731–2746.
[46] E.O. Knutson, K.T. Whitby, Aerosol classification by electric mobility: apparatus, theory, and applications, J. Aerosol Sci. 6 (1975) 443–451.
[47] C. Larriba, C.J. Hogan, M. Attoui, R. Borrajo, J.F. Garcia, J.F. de la Mora, The mobility-volume relationship below 3.0 nm examined by tandem mobility-mass measurement, Aerosol Sci. Technol. 45 (2011) 453–467.
[48] C.N. Davies, Definitive equations for the fluid resistance of spheres, Proc. Phys. Soc. 57 (1945) 259–270.
[49] J.M. Thomas, S. He, C. Larriba-Andaluz, J.W. DePalma, M.V. Johnston, C.J. Hogan, Ion mobility spectrometry-mass spectrometry examination of the structures, stabilities, and extents of hydration of dimethylamine-sulfuric acid clusters, Phys. Chem. Chem. Phys. 18 (2016) 22962–22972.
[50] C. Larriba-Andaluz, J. Fernandez-Garcia, M.A. Ewing, C.J. Hogan, D.E. Clemmer, Gas molecule scattering & ion mobility measurements for organic macro-ions in He versus N-2 environments, Phys. Chem. Chem. Phys. 17 (2015) 15019–15029.
[51] H. Ouyang, C. Larriba-Andaluz, D.R. Oberreit, C.J. Hogan, The collision cross sections of iodide salt cluster ions in air via differential mobility analysis-mass spectrometry, J. Am. Soc. Mass Spectrom. 24 (2013) 1833–1847.
[52] C. Zhang, T. Thajudeen, C. Larriba, T.E. Schwartzentruber, C.J. Hogan, Determination of the scalar friction factor for nonspherical particles and aggregates across the entire knudsen number range by direct simulation monte carlo (DSMC), Aerosol Sci. Technol. 46 (2012) 1065–1078.
[53] T. Thajudeen, S. Jeon, C.J. Hogan, The mobilities of flame synthesized aggregates/agglomerates in the transition regime, J. Aerosol Sci. 80 (2015) 45–57.
[54] S.N. Rogak, R.C. Flagan, H.V. Nguyen, The mobility and structure of aerosol agglomerates, Aerosol Sci. Technol. 18 (1993) 25–47.
[55] W. Li, D.-R. Chen, Performance of nano-DMA operated with different gases for sheath and aerosol carrier flows, Aerosol Sci. Technol. 39 (2005) 931–940.
[56] G.R. Markowski, Improving twomey's algorithm for inversion of aerosol measurement data, Aerosol Sci. Technol. 7 (1987) 127–141.
[57] L. Li, H.S. Chahl, R. Gopalakrishnan, Comparison of the predictions of langevin dynamics-based diffusion charging collision kernel models with canonical experiments, J. Aerosol Sci. 140 (2020) 105481.
[58] A. Wiedensohler, An approximation of the bipolar charge-distribution for particles in the sub-micron size range, J. Aerosol Sci. 19 (1988) 387–389.
[59] T. Seto, T. Orii, M. Hirasawa, N. Aya, H. Shimura, Ion beam charging of silicon nanoparticles in helium background gas: design of the ion beam aerosol charger, Rev. Sci. Instrum. 74 (2003) 3027–3030.
[60] T. Seto, T. Orii, H. Sakurai, M. Hirasawa, S.-B. Kwon, Ion beam charging of aerosol nanoparticles, Aerosol Sci. Technol. 39 (2005) 750–759.
[61] C.H.I. Tien, C.-S. Wang, D.T. Barot, Chainlike formation of particle deposits in fluid-particle separation, Science 196 (1977) 983.
[62] M.Y. Manuputty, C.S. Lindberg, M.L. Botero, J. Akroyd, M. Kraft, Detailed characterisation of TiO2 nano-aggregate morphology using TEM image analysis, J. Aerosol Sci. 133 (2019) 96–112.
[63] M. Frei, F.E. Kruis, Image-based size analysis of agglomerated and partially sintered particles via convolutional neural networks, Powder Technol. 360 (2020) 324–336.
[64] A.V. Filippov, M. Zurita, D.E. Rosner, Fractal-like aggregates: relation between morphology and physical properties, J. Colloid Interf. Sci. 229 (2000) 261–273.
[65] M. van Sebille, L.J.P. van der Maaten, L. Xie, K. Jarolimek, R. Santbergen, R.A.C.M.M. van Swaaij, K. Leifer, M. Zeman, Nanocrystal size distribution analysis from transmission electron microscopy images, Nanoscale 7 (2015) 20593–20606.
[66] R. Dastanpour, J.M. Boone, S.N. Rogak, Automated primary particle sizing of nanoparticle aggregates by TEM image analysis, Powder Technol. 295 (2016) 218–224.
[67] S. Jeon, K.R. Hurley, J.C. Bischof, C.L. Haynes, C.J. Hogan, Quantifying intra- and extracellular aggregation of iron oxide nanoparticles and its influence on specific absorption rate, Nanoscale 8 (2016) 16053–16064.
[68] R. Gopalakrishnan, T. Thajudeen, C.J. Hogan, Collision limited reaction rates for arbitrarily shaped particles across the entire diffusive Knudsen number range, J. Chem. Phys. 135 (2011) 54302.
[69] R.D. Mountain, G.W. Mulholland, Light scattering from simulated smoke agglomerates, Langmuir 4 (1988) 1321–1326.
[70] P. Meakin, R. Jullien, The effects of restructuring on the geometry of clusters formed by diffusion-limited, ballistic, and reaction-limited cluster–cluster aggregation, J. Chem. Phys. 89 (1988) 246–250.
[71] D.A. Weitz, M. Oliveria, Fractal structures formed by kinetic aggregation of aqueous gold colloids, Phys. Rev. Lett. 52 (1984) 1433–1436.
[72] M.Y. Lin, H.M. Lindsay, D.A. Weitz, R.C. Ball, R. Klein, P. Meakin, Universality in colloid aggregation, Nature 339 (1989) 360–362.
[73] T. Thajudeen, S. Deshmukh, C.J. Hogan, Langevin simulation of aggregate formation in the transition regime, Aerosol Sci. Technol. 49 (2015) 115–125.
[74] C. Janzen, H. Kleinwechter, J. Knipping, H. Wiggers, P. Roth, Size analysis in low-pressure nanoparticle reactors: comparison of particle mass spectrometry with in situ probing transmission electron microscopy, J. Aerosol Sci. 33 (2002) 833–841.
[75] G.J. Lindquist, D.Y.H. Pui, C.J. Hogan Jr., Porous particulate film deposition in the transition regime, J. Aerosol Sci. 74 (2014) 42–51.

[76] W. Aigner, O. Bienek, B.P. Falcão, S.U. Ahmed, H. Wiggers, M. Stutzmann, R.N. Pereira, Intra- and inter-nanocrystal charge transport in nanocrystal films, Nanoscale 10 (2018) 8042–8057.
[77] Q. Chen, J.R. Guest, E. Thimsen, Visualizing current flow at the mesoscale in disordered assemblies of touching semiconductor nanocrystals, J. Phys. Chem. C 121 (2017) 15619–15629.
[78] X. Chen, V. Gandhi, J. Coots, Y. Fan, L. Xu, N. Fukushima, C. Larriba-Andaluz, High resolution varying field drift tube ion mobility spectrometer with diffusion autocorrection, J. Aerosol Sci. 140 (2020) 105485.
[79] L. Deng, I.K. Webb, S.V.B. Garimella, A.M. Hamid, X. Zheng, R.V. Norheim, S.A. Prost, G.A. Anderson, J.A. Sandoval, E.S. Baker, Y.M. Ibrahim, R.D. Smith, Serpentine ultralong path with extended routing (SUPER) high resolution traveling wave ion mobility-MS using structures for lossless ion manipulations, Anal. Chem. 89 (2017) 4628–4634.
[80] M. Domaschke, C. Lübbert, W. Peukert, Analysis of ultrafine metal oxide particles in aerosols using mobility-resolved time-of-flight mass spectrometry, J. Aerosol Sci. 137 (2019) 105438.